https://doi.org/10.5194/acp-2021-257
Preprint. Discussion started: 17 May 2021

Atmospheric Chemistry and Physics Discussions

Investigation of near-global daytime boundary layer height using high-resolution radiosondes: First results and comparison with ERA-5, MERRA-2, JRA-55, and NCEP-2 reanalyses

Jianping Guo[a], Jian Zhang[b], Kun Yang[c], Hong Liao[d], Shaodong Zhang[e], Kaiming Huang[e],Yanmin Lv[a], Jia Shao[f], Tao Yu[b], Bing Tong[a], Jian Li[a], Tianning Su[g], Steve H.L. Yim[h,i], Ad Stoffelen[j], Panmao Zhai[a], and Xiaofeng Xu[k]

[a] State Key Laboratory of Severe Weather, Chinese Academy of Meteorological Sciences, Beijing 100081, China

[b] Hubei Subsurface Multi-scale Imaging Key Laboratory, Institute of Geophysics and Geomatics, China University of Geosciences, Wuhan 430074, China

[c] Department of Earth System Science, Tsinghua University, Beijing 100084, China

[d] Nanjing University of Information Science and Technology, Nanjing 210044, China

[e] School of Electronic Information, Wuhan University, Wuhan 430072, China

[f] College of Informatics, Huazhong Agricultural University, Wuhan 430070, China

[g] Department of Atmospheric and Oceanic Sciences, University of Maryland, College Park, Maryland 20740, USA

[h] Department of Geography and Resource Management, The Chinese University of Hong Kong, Shatin, Hong Kong, China

[i] Stanley Ho Big Data Decision Analytics Research Centre, The Chinese University of Hong Kong, Shatin, Hong Kong, China

[j] The Royal Netherlands Meteorological Institute (KNMI), 3730 AE De Bilt, The Netherlands

[k] China Meteorological Administration, Beijing 100081, China

Correspondence to:
Dr. Jian Zhang (Email: zhangjian@cug.edu.cn)

https://doi.org/10.5194/acp-2021-257
Preprint. Discussion started: 17 May 2021

Atmospheric Chemistry and Physics Discussions

Abstract

The planetary boundary layer height (BLH) governs the vertical transport of mass, momentum and moisture between the surface and the free atmosphere, and thus its characterization is recognized as crucial for air quality, weather and climate. Although reanalysis products can provide important insight into the global view of BLH in a seamless way, the in situ observed BLH on a global scale remains poorly understood due to the lack of high-resolution (1-s or 2-s) radiosonde measurements. The present study attempts to establish a near-global BLH climatology at synoptic times (0000 and 1200 UTC) and in the daytime using high-resolution radiosonde measurements over 300 radiosonde sites worldwide for the period 2012 to 2019, which is then compared against the BLHs obtained from four reanalysis datasets, including ERA-5, MERRA-2, JRA-55, and NCEP-2. The variations of BLH exhibit large spatial and temporal dependence, and as a result the BLH maxima are generally discerned over the regions such as Western United States and Western China, in which the balloon launch times mostly correspond to the afternoon. The diurnal variations of BLH are revealed with a peak at 1700 Local Solar Time (LST). The most promising reanalysis product is ERA-5, which underestimates BLH by around 130 m as compared to radiosondes. In addition, MERRA-2 is a well-established product and has an underestimation of around 160 m. JRA-55 and NCEP-2 might produce considerable additional uncertainties, with a much larger underestimation of up to 400 m. The largest bias in the reanalysis data appears over the Western United States and Western China and it might be attributed to the maximal BLH in the afternoon when the boundary layer has grown up. Statistical analyses further indicate that the biases of reanalysis BLH products are positively associated with orographic complexity, as well as the occurrence of static instability. To our best knowledge, this study presents the first near-global view of high-resolution radiosonde derived BLH and provides a quantitative assessment of the four frequently used reanalysis products.

Keywords. Radiosonde; boundary layer height; reanalysis; sensible heat flux

https://doi.org/10.5194/acp-2021-257
Preprint. Discussion started: 17 May 2021


Atmospheric Chemistry and Physics Discussions

1. Introduction

The planetary boundary layer (PBL) and its evolution has a profound influence on research fields such as air quality (Stull, 1988; Li *et al.,* 2017), boundary layer cloud and fog (Liu and Liang, 2010), convective storm (Oliveira *et al*., 2020) and global warming (Davy and Esau, 2016), among others. It is well known to be influenced by radiative cooling at night and by downward solar radiation reaching the ground surface at daytime, respectively, forming a stable boundary layer (SBL) and convective boundary layer (CBL), with a typical boundary layer depth (BLH) of less than 500 m and 1–3 km (Zhang *et al.,* 2020a), respectively. For climate models, most of the PBL processes occur at sub-grid scales and thus are either underrepresented or not fully represented (von Engeln and Teixeira, 2013). Meanwhile, there are many problems in elucidating the PBL processes using numerical model simulations (Martins *et al.,* 2010), even over the relatively homogeneous ocean (Belmonte and Stoffelen, 2019), which is likely due to the scarcity of fine-scale vertical observations of the atmosphere.

Over the oceans Belmonte and Stoffelen (2019) performed a climatological comparison between state-of-the-art reanalysis and scatterometer surface winds in the PBL, revealing mean and transient PBL model errors. Houchi *et al.* (2010), based on high-resolution radiosondes, verified the climatological wind profiles and found in particular a factor of 2–3 lower wind shear simulated by the European Centre for Medium-Range Weather Forecasts (ECMWF) model. Wind shear is recognized to be able to significantly modulate turbulent mixing of atmospheric pollutants (Zhang *et al.,* 2020b), and thus the inabilities of the model in this regard may have repercussions for air quality prediction.

The temporal and spatial variations in BLH have been extensively assessed in previous studies at a regional or national scale, such as the contiguous United States (Seidel *et al.,* 2012; Zhang *et al.,* 2020a), Europe (Palarz *et al*., 2018), China (Guo *et al.,* 2016; Zhang *et al*., 2018, Su *et al*., 2018), Arctic and Antarctic (Zhang *et al*., 2011), which are mainly implemented by radiosonde measurements, reanalysis or both. And

https://doi.org/10.5194/acp-2021-257
Preprint. Discussion started: 17 May 2021


Atmospheric Chemistry and Physics Discussions

notable diurnal and seasonal cycles have been revealed (e.g., Guo *et al.,* 2016; Short *et al.,* 2019). Besides the regional results, several attempts have been made to provide global-scale retrievals of BLH using the Global Positioning System radio occultation (GPS RO) and Integrated Global Radiosonde Archive (IGRA) version 2 (Seidel *et al.,* 2010; Gu *et al.,* 2020; Ratnam and Basha, 2010), in which seasonal variations and maritime-continental contrasts of BLHs have been achieved. The measurements of GPS RO, at a vertical resolution of 100 m around the PBL top, are typically used to determine BLH by searching for the altitude with a sharp gradient in the refractivity profile (Basha *et al.,* 2018). However, such sharp gradient of refractivity might overestimate BLH compared to other methods that the community usually used, such as the parcel method (Seidel *et al.,* 2010). Compared with high-resolution soundings, IGRA is sparsely sampled in the vertical, which could result in large uncertainties in estimating BLH. Likewise, additional errors could be introduced in reanalysis products for their sparse vertical resolutions, which are equivalent to or bigger than IGRA. A large spread emerges in the explicit determination of BLH from a variety of instruments, in spite of that the BLH detection based on radiosonde is the most accepted methodology for deriving CBL and SBL (Seidel *et al.,* 2012; de Arruda Moreira *et al.,* 2018).

A wide range of reanalysis products, such as those from the fifth generation ECMWF atmospheric reanalysis of the global climate (ERA-5), the National Aeronautics and Space Administration (NASA) Modern-Era Retrospective-analysis for Research and Applications version 2 (MERRA-2), Japanese 55-year Reanalysis (JRA-55), and the NCEP climate forecast system version 2 (NCEP-2), provide a rich ensemble of climate data products (Saha *et al.,* 2014; Hersbach *et al.,* 2020; Kobayashi *et al.,* 2015; Gelaro *et al.,* 2017), but are sensitive to both empirical parameterizations and the diagnostic method chosen, while verification by direct observations of BLH are sparse (Seibert *et al.,* 2000). Some inter-comparisons between instruments, such as radiosonde, LIDAR, and ERA-interim reanalysis have been previously conducted, and a rough consistency has been yielded (e.g., Guo *et al.,* 2016; Korhonen *et al.,* 2017; Zhang *et al.,* 2016). However, Basha *et al.* (2018) demonstrate that ERA-interim can

https://doi.org/10.5194/acp-2021-257
Preprint. Discussion started: 17 May 2021


Atmospheric Chemistry and Physics Discussions

underestimate BLH by around 900 m compared to GPS RO. This underestimation may be caused by different kinetic or thermodynamic assumptions use. For instance, ERA-interim is implemented with a bulk Richardson number method (Palm *et al.,* 2005), which is believed to be suitable for all atmospheric conditions (Anderson, 2009). It is worth highlighting that the state-of-art reanalysis could be one of the most promising data sources for obtaining the synoptic or climatological features of BLH.

Despite much progress made in developing the BLH products, there are still some unresolved issues in quantifying the variability of BLH from a global perspective. These issues include: the worldwide variation of BLH by high-resolution vertical soundings, the inter-comparisons among reanalysis datasets, and further evaluations with radiosonde observations, especially in the daytime based on the same retrieval algorithm. To this end, this study seeks to address the following scientific questions: (1) a climatological distribution of near-global BLH by using high-resolution radiosonde measurements; (2) inter-comparisons of ERA-5, MERRA-2, JRA-55, and NCEP-2 with additional evaluation with radiosondes; and (3) investigate potential sources for the biases of BLH between observation and reanalysis. The rest of the paper is organized as follows. The descriptions of high-resolution radiosonde data, reanalysis products, and the bulk Richardson number method are given in Section 2. Section 3 presents the spatial distributions of BLH by radiosonde and reanalyses and their inter-comparisons. A brief conclusion and remarks are finally outlined in Section 4.

2. Data descriptions and BLH retrieval method

2.1 High-resolution radiosonde measurements

Until January 2018, IGRA provided atmospheric soundings at around 445 radiosonde sites across the globe, including pressure, temperature, humidity and wind. The number of pressure levels below 500 hPa is around 10. By comparison, for high-resolution radiosondes, the sampling rate is 1-s or 2-s, corresponding to a vertical resolution of approximately 5–10 meters throughout the atmosphere. The high-

https://doi.org/10.5194/acp-2021-257
Preprint. Discussion started: 17 May 2021


Atmospheric Chemistry and Physics Discussions

resolution radiosonde measurements used in the present study are obtained from 342 sites around the world, which are provided by several organizations, including the China Meteorological Administration (CMA), the National Oceanic and Atmospheric Administration (NOAA) of United States, the German Deutscher Wetterdienst (Climate Data Center), the Centre for Environmental Data Analysis (CEDA) of United Kingdom, the Global Climate Observing System (GCOS) Reference Upper Air Network (GRUAN), and University of Wyoming.

The CMA maintains the China Radiosonde Network (CRN), which contains 120 operational stations homogeneously distributed across mainland China with a vertical sampling rate of 1 second (5–8 m resolution), since 2011 (Guo *et al.,* 2016; 2019; Zhang *et al.,* 2016; 2018; Su *et al.,* 2020). The NOAA started the Radiosonde Replacement System (RRS) program in 2005, which involved 89 sites with a vertical resolution of 5 m (Zhang *et al.,* 2019). The German Deutscher Wetterdienst (Climate Data Center) has been sharing the radiosonde measurements at 14 sites with a sampling rate of 2 seconds since 2010. Moreover, the 10 m resolution soundings at 12 sites was provided by the CEDA, which began to share soundings since 1990, and 8 radiosonde sites were shared by GRUAN with a vertical resolution smaller than 10 m. An additional 93 sites came from the University of Wyoming, which started in 2018, with a sampling rate of 2-s or 1-s. In total, over 678,000 soundings at 342 stations are used here for the period of January 2012 to December 2019 in total of eight years, including 633,000 soundings at the regular release times of 0000 and 1200 UTC and 43,000 more irregular observations during intensive observation period (IOP).

Radiosonde measurements are taken twice per day following the World Meteorological Organisation (WMO) protocol for synoptic times at 0000 and 1200 UTC (Seibert *et al.,* 2000), except for special field campaign observations at specified stations or time ranges during IOPs. The protocol implies that stations at different longitudes sample the diurnal cycle differently. For instance, stations near 0°E (London) and 180°E (Samoa) sample at midnight and midday, while stations near 90°E (Bangladesh) and 90°W (Chicago) sample at dawn and dusk, with intermediate

https://doi.org/10.5194/acp-2021-257
Preprint. Discussion started: 17 May 2021


Atmospheric Chemistry and Physics Discussions

longitudes at linearly varying intermediate local solar times (LSTs) of day. For wintertime regions near 90°W and 90°E, the release times are insufficient for evaluating the BLH during daytime. Hence, the BLH estimates from regular radiosondes will vary with longitude and season (McGrath-Spangler and Denning, 2012). Generally, the principal PBL mechanism at night is associated with an SBL, which gradually transitions into CBL in the morning (Stull, 1988; Zhang *et al.,* 2018). The transition from SBL to CBL is generally quick and occurs swiftly after sunrise, but the reverse process can be slow in the late evening (Taylor *et al.,* 2014). Despite the dominance of CBL during the daytime, an SBL still occurs, especially in the event of overcast sky (Zhang *et al.,* 2018; 2020) and near strong divergence in moist convective downbursts (King *et al.,* 2017). To illustrate the daytime variation of BLH, we only selected the soundings that are launched 2 hours after sunrise and 2 hours before sunset. The sunrise and sunset times are gauged in a longitude bin size of 15 degrees and based on the latitude of station and the calendar day of the release. As a result, 190,013 profiles which include soundings launched at both synoptic times and during IOP, spanning from January 2012 to December 2019, to obtain the BLH in the daytime. The spatial distribution of file number for each site is displayed in Figure S1, in which the sites with less than 10 matches are excluded.

2.2 ERA-5, MERRA-2, JRA-55 and NCEP-2 reanalysis datasets

ERA-5 is the successor of ERA-interim and undergo a variety of improvements, including more recent parameterization schemes and data assimilation system, better spatial resolution, both horizontally and vertically (137 levels), and improved representation of evaporation balance, cyclones, soil moisture, and global precipitation (Hersbach *et al.,* 2020). The BLH is composited in the ERA-5 product on a 1440×721 grids with 0.25° longitude and 0.25° latitude resolution. It is computed by the bulk Richardson number method, with a temporal resolution of 1 hour.

MERRA-2 is the latest atmospheric reanalysis of the modern satellite era produced by NASA's Global Modeling and Assimilation Office (GMAO). It includes aerosol data assimilation, improvements on ozone, and cryospheric processes (Gelaro

https://doi.org/10.5194/acp-2021-257
Preprint. Discussion started: 17 May 2021


Atmospheric Chemistry and Physics Discussions

et al., 2017). The data is provided on a grid of 576×361 points with 0.625° longitude and 0.5° latitude resolution and has 42 pressure levels (about 16 layers below 500 hPa), with a temporal resolution of 3 h. In this product, the BLH is defined by identifying the lowest level at which the heat diffusivity drops below a threshold value (McGrath-Spangler and Denning, 2012). However, to preclude the uncertainty raised by different methods adopted, the BLH by MERR-2 is extracted by bulk Richardson number method, utilizing the parameters of horizontal wind, temperature, geopotential height, relative humidity (RH), and surface pressure.

JRA-55 is the second Japanese global atmospheric reanalysis commissioned by the Japan Meteorological Agency (JMA) (Kobayashi *et al.,* 2015). Data contains 37 pressure levels between 1 hPa and 1000 hPa (16 layers below 500 hPa), provided on a grid of 288×145 points, with a horizontal spacing of 1.25°×1.25° and a temporal resolution of 6 hours. The parameters, including geopotential height, temperature, horizontal wind, surface pressure, and RH, are used to assess BLH as before. NCEP-2 has the coarsest model resolution than ERA-5 (Rinke *et al.,* 2019), with a spatial resolution of 2.5° longitude and 2.5° latitude. The total level is 17 (6 layers below 500 hPa), which is substantially less than MERRA-2, JRA-55 or ERA-5, and the temporal resolution is 6 hours. Similar parameters to JRA-55 are preserved to compute BLH. It is noteworthy that all model times include 00 and 12 UTC and hence collocate well with the synoptic radiosonde times.

2.3 Normalized sensible heat flux in the daytime

The sensible heat flux represents the level of energy that induces CBL growth (Wei *et al*., 2017), whereas the latent heat fluxes characterize the evaporation of moisture from the soil to the CBL, which feedbacks on the development of CBL and the formation of PBL cloud (Pal and Haeffelin, 2015) For a given amount of heat flux, small latent heat fluxes usually mean more energy being available for PBL growth (Chen *et al*., 2016). Moreover, the surface heat flux is closely associated with near-surface meteorological variables. For instance, a lower RH usually indicates a larger sensible heat flux and lower latent heat flux (Guo *et al*., 2019; Zhang *et al*., 2013).

https://doi.org/10.5194/acp-2021-257
Preprint. Discussion started: 17 May 2021


Atmospheric Chemistry and Physics Discussions

Suppose that the heat supplied to the air at the radiosonde balloon launch time is the area shaded under the heat flux curve (Fig.11.12 in Stull 1988), the normalized sensible heat flux in the daytime is defined by

$$\overline{Q_H} \propto \int_{T_{sunrise}}^{T_{launch}} Q_H \rho^{-1} c_p^{-1} dt \quad (1)$$

where $T_{sunrise}$ and T_{launch} are the sunrise time and radiosonde balloon launch time, Q_H the sensible heat flux, ρ the near-surface density and c_p equals 1004 J°C$^{-1}kg^{-1}$. The similar principle is applied to the calculation of normalized latent sensible heat flux as well.

2.4 Bulk Richardson number method

In the spirits of a like-for-like comparison, the BLHs derived from radiosonde and reanalysis data (MERRA-2, JRA-55, and NCEP-2) are calculated using the bulk Richardson number (BRN), which also serves as the built-in algorithm in ERA-5 for BLH products. The BRN, an algorithm used to reflect how strongly buoyancy is coupled to the vertical momentum (Scotti, 2015), has been widely used for the climatological study of BLH from radiosonde measurements thanks to its applicability and reliability for all PBL regimes (Anderson 2009; Seidel *et al.,* 2012; Guo *et al.,* 2019). It determines the BLH by identifying the level at which the bulk Richardson number, represented by $Ri(z)$, reaches its critical value (Palm *et al.*, 2005) and is formulated as

$$\mathrm{Ri(z)} = \frac{\left(\frac{g}{\theta_{vs}}\right)(\theta_{vz}-\theta_{vs})z_{AG}}{(u_z-u_s)^2+(v_z-v_s)^2+(bu_*^2)} \quad (2)$$

where g is the gravitational acceleration, z_{AG} the height above ground level (AGL), θ_v the virtual potential temperature, u_* the surface friction velocity, and u and v the horizontal wind components and b a constant, which is usually set to zero due to the fact that friction velocity is much weaker compared with the horizontal wind (Seidel *et al.*, 2012). The subscripts of z and s denote the parameters at z height above ground and ground level, respectively.

https://doi.org/10.5194/acp-2021-257
Preprint. Discussion started: 17 May 2021


Atmospheric Chemistry and Physics Discussions

It is known that $Ri(z)$ increases with increasing free flow stability (Zilitinkevich and Baklanov, 2002). Below a critical value of 0.25, the flow is dynamically unstable and likely cause turbulent motion. Nevertheless, since turbulence can also occur away from this critical value (Haack *et al.,* 2014), care must be taken in that the critical value might not be well defined, leading to uncertainty in estimating BLH. Meanwhile, the BLH estimates were found not to change very much by differing the input of critical values ($Ri = 0.2; 0.25; 0.3$) (Guo *et al.,* 2016). Therefore, for a given discrete Ri profile, here we identify the BLH as the interpolated height at which the $Ri(z)$ firstly crosses the critical value of 0.25 starting upward from the ground surface.

2.5 Collocation procedure and a case study

In contrast to the reanalysis data, the longitude, and latitude distributions of high-resolution radiosonde are irregular. A precise comparison between reanalysis data and sounding is required for consistency in time, latitude, and longitude. The matching procedures implemented in this present study go as follows. (1) A latitudinal and longitudinal matching procedure is carried out by finding the geographical grid cell of the reanalysis product that contains the radiosonde station. (2) Time matching for ERA-5 is to find the exact UTC time (hour) of the weather balloon launch. (3) For MERRA-2, NCEP-2, and JRA-55 datasets, the requirement is to limit the time difference with the weather balloon launch time to 1 hour.

A case at 0600 UTC 06 Jun 2016, Chongqing (29.6°N, 106.4°E) is shown in Figure 1. In this case, BLH obtained by sounding is 1,337 m and is closest to that by ERA-5, which underestimates the height by 72 m. Compared with the radiosonde profile, MERRA-2 can capture the main vertical structures and the magnitude of wind speed (WS), RH, and temperature, but not the fine-scale vertical variations (Figure 1b). It also slightly undervalues the BLH by 125 m. By and large, the profiles from JRA-55 are not as accurate as those from MERRA-2. More specifically, the wind speed at some heights, prominently above 2 km, is underestimated (Figure 1d); the mean RH is 4% less than that from the sounding. As a result, JRA-55 substantially underestimates BLH by 399 m. The basic parameters outlined by NCEP-2, for instance, RH (5% larger than

https://doi.org/10.5194/acp-2021-257
Preprint. Discussion started: 17 May 2021


Atmospheric Chemistry and Physics Discussions

285 sounding), temperature (3°C less than sounding), and wind speed (4.5 m/s larger than
286 sounding), all have notable differences with the sounding (Figure 1c). The BLH is
287 considerably underestimated by 729 m. Based on this case, we can note that the
288 performances of ERA-5 and MERRA-2 are obviously better than those from JRA-55
289 and NCEP-2 in terms of the BLH, and that the remarkable underestimation by NCEP-
290 2 can be attributed to the large error in the prediction of basic parameters, such as wind,
291 temperature, and RH.

292 3. Results and discussion

293 *3.1 Overview of BLHs at two synoptic times*

294 The near-global mean BLHs at 0000 UTC from 2012 to 2019 by four reanalysis
295 products are shown in Figure 2, in which the results obtained from radiosonde are
296 overlaid by colored circles. The stations with sounding covering at least 2 continuous
297 years are kept. The four reanalysis products yield an analogous result with respect to
298 the spatial variation of BLHs, which are positively correlated with the sounding-derived
299 BLH, with correlation coefficients of 0.90, 0.47, 0.46, 0.81 for ERA-5, NCEP-2, JRA-
300 55, and MERRA-2, respectively. It is evident that the BLHs from NCEP-2 over the
301 continents of Africa, Asia, and South America are 300 m thicker than those of the other
302 three products (Figure 2b). Furthermore, the BLH in Antarctic by ERA-5 is notably 500
303 m lower than that by NCEP-2 and MERRA-2 (Figure 2a). Most of the mean BLHs by
304 radiosonde are consistent with the reanalysis products, except that the values from all
305 four reanalysis products over the Pacific Ocean and the contiguous U.S. are
306 underestimated by about 300 m. Moreover, it is worth to note here that the BLHs by
307 JRA-55 are considerably underestimated by around 1 km over these regimes. For 0000
308 UTC, the regions nearly from the east coast to the west coast of Pacific Ocean (UTC+8
309 to UTC+12, and UTC–12 to UTC–8) are covered by sunshine, and thus are filled with
310 deeper PBL.

https://doi.org/10.5194/acp-2021-257
Preprint. Discussion started: 17 May 2021


Atmospheric Chemistry and Physics Discussions

311 Comparable results at 1200 UTC are presented in Figure S2. Africa, the Middle
312 East, and the west of India and China, corresponding to local noon and afternoon, have
313 maximal BLHs of around 1.8 km. Moreover, it is noteworthy that the values from
314 NCEP-2 and JRA-55 over these areas are visibly lower than those from ERA-5 and
315 MERRA-2, particularly over Africa and the Middle East, whereas these low values can
316 barely be validated with soundings due to their sparse distribution. Over these areas,
317 the BLHs are underestimated by reanalysis by about 200 m relative to the sounding
318 results. Notably, BLHs from NCEP-2 over the continents of Africa are 1 km lower than
319 those from ERA-5 and MERRA-2. According to the results at 0000 and 1200 UTC, the
320 comparisons between reanalysis products and soundings demonstrate that the BLHs are
321 well resolved in the nighttime but are underestimated at daytime by reanalysis datasets.

322 For the near-global variation of BLH at a certain synoptic time, daytime and
323 nighttime appear on the map simultaneously, but as a function of longitude, which is
324 displayed in Figure 2. Thus, the variations at a fixed synoptic time on the map create a
325 picture of the diurnal BLH variation. Given the dominance of CBL in the daytime,
326 investigating the BLHs in the daytime is thus favorable for unravelling the underlying
327 causes for the discrepancies existed in the BLHs from both radiosonde and reanalysis.
328 Therefore, the following results show the variations of daytime BLH only, unless
329 otherwise noted.

330 *3.2 Variations over the day and comparisons with reanalysis products*

331 The climatological mean variations in the daytime BLH from the soundings and
332 four reanalysis products are drawn in Figure 3. The period spans from January 2012 to
333 December 2019 for most of the stations provided by China, the U.S., Germany, and the
334 U.K. As implied by the results from soundings (Figure 3e), the deepest PBL is observed
335 over the Tibetan Plateau (TP) and the northwest of China, the south of Africa, and the
336 west of U.S, with values as high as 1.7 km. The possible reason for this phenomenon is
337 that the weather balloons over these regions are basically launched in the early
338 afternoon of boreal summer (June–July–August) when the maximal BLH is usually
339 observed (Collaud Coen *et al.,* 2014; Guo *et al.,* 2016). The BLHs over the Pacific

https://doi.org/10.5194/acp-2021-257
Preprint. Discussion started: 17 May 2021


Atmospheric Chemistry and Physics Discussions

Ocean are noticeably large, with values of 1.3 km. The longitudinal variation of BLH is evident, likely due to LST variations of the soundings. Additionally, BLHs in the middle and low latitudes are larger than high latitudes, which is consistent with the findings in Gu *et al.* (2020).

By and large, the climatological results of BLH by radiosonde and four model products are comparable, indicating that both capture the diurnal and seasonal variations implied by the sounding LST times sampled. Among the model products, ERA-5 shows the best prediction of BLH contrasted with radiosonde, with a correlation coefficient of 0.88 (Figure 3a). Furthermore, the results from MERRA-2 are positively correlated with those from the soundings, with a correlation coefficient of 0.66 (Figure 3b). The performances of JRA-55 and NCEP-2 are significantly poorer than those of ERA-5 and MERRA-2, with correlation coefficients of 0.4 and 0.41, respectively (Figure 3c, d). The values of BLH over the west of U.S and the west of China are seriously underestimated by NCEP-2 and JRA-55 by around 800 m. Thus, we note that ERA-5 and MERRA-2 are more robust in deriving the BLH, purely based on the climatological distribution of BLHs.

Figure 4 illustrates the diurnal variations in BLH at 0000 and 1200 UTC and during daytime. A notable diurnal variation can be noticed, with a minimum of 343 m at 04 LST and a maximum of 1224 m at 17 LST (Figure 4a). The magnitude in BLH during daytime are essentially larger than that at 0000 and 1200 UTC and has a maximal value of 1926 m at 1700 LST (Figure 4b). It follows that some soundings that are released at 0000 and 1200 UTC are excluded by the collocation procedure designed for collecting samples in the daytime.

The radiosonde stations are mainly dispersed over the U.S, China, Austria, Europe, the Pacifica Ocean, and the polar region, and only a few stations contribute over the rest of the world. The polar region contains a station with a longitude larger/lower than 67.7°N/°W. Therefore, six regions are specifically examined in terms of the bias between radiosonde and model product.

https://doi.org/10.5194/acp-2021-257
Preprint. Discussion started: 17 May 2021


Atmospheric Chemistry and Physics Discussions

368 The BLH differences between radiosonde and ERA-5 are shown in Figure 5, in
369 which we specify the differences over the six above-mentioned regions. As observed in
370 Figure 5e, the BLH over most of the stations is underestimated to a slight extent, with
371 a near-global mean of 130.44 m. As expected, the most underestimated regions cover
372 the west of U.S, and southern China (Figure 5e), with a difference of around 200 m. In
373 addition, it is worth mentioning that the BLHs over the Pacific Ocean are overestimated
374 in four seasons, with a bias of around 400 m (Figure 5h). Among the six classified
375 regions, BLHs in Europe, East Asia, and polar are reliably determined by ERA-5, with
376 an average bias of around 50 m (Figure 5b, c, i). The bias seems to exhibit a seasonal
377 dependence, and it is larger in the warm seasons and smaller in the cool seasons.
378 Regardless of the small bias, the newest model product, ERA-5, properly estimates the
379 BLH, especially above the regions of Europe, the eastern U.S, East Asia, and polar.

380 Similarly, the BLHs by MERRA-2 are underestimated, with a near-global mean
381 bias of 159.72 m (Figure 6), which is slightly larger than that of ERA-5 (130.44 m).
382 This could indicate that the MERR-2-derived BLH is more dispersed than ERA-5. The
383 spatial distribution of bias value is broadly identical to that of ERA-5, except that the
384 BLHs over Europe, Austria, and polar region are well estimated by MERR-2, due to
385 much smaller mean biases at 42.10 m, 39.70/. m, and 52.27 m, respectively (Figure 6b,
386 g, i).

387 By comparison, the mean bias produced by JRA-55 is larger than those from ERA-
388 5 and MERRA-2, with a mean value of 352.59 m, as shown in Figure 7. The BLHs
389 above most stations are underestimated by JRA-55, particularly for the sites over
390 western China and western U.S, and the Pacific Ocean, with an underestimation of
391 about 800 m. The most underestimated stations cluster at the latitude range of 40–45°N,
392 with a mean difference of around 1 km (Figure 7f). Although the ensemble mean of
393 bias is significantly larger than ERA-5 and MERRA-2, the estimations over Europe and
394 the Polar regions seem to be acceptable, with mean values of 177.0 m and 99.2 m,
395 respectively (Figure 7b, i).

https://doi.org/10.5194/acp-2021-257
Preprint. Discussion started: 17 May 2021


Atmospheric Chemistry and Physics Discussions

396 The mean bias by NCEP-2 is larger than that by JRA-55, with a mean value of
397 420.87 m, as illustrated by Figure 8. The distribution results are similar to JRA-55,
398 except for Europe and Austria, where the bias is about twice that of JRA-55.

399 In general, the comparison analysis of the daytime BLH results between soundings
400 and four reanalysis datasets indicates that ERA-5 reanalysis produces the BLH that is
401 closest to the high-resolution soundings. Interestingly, MERRA-2 can provide a good
402 spatial distribution of BLH. JRA-55 and NCEP-2 can only give a good prediction over
403 some regions, most of which tends to produce a much larger BLH estimates compared
404 to those from ERA-5 and MERRA-2.

405 *3.3 Correlations with near-surface meteorological variables and surface heat flux*

406 The PBL is the lowest part of the troposphere and evolves diurnally due to near-
407 surface thermodynamic variables through turbulent exchanges of momentum, heat, and
408 moisture (Pithan *et al*., 2015). Thus, the surface meteorological variables depend on the
409 underlying land surface and its coupling with the PBL, and they could act as a good
410 proxy for BLH under some specific circumstances (Zhang *et al*., 2013; Zhang *et al*.,
411 2018). An analysis of the correlation between the BLHs by radiosondes and near-
412 surface meteorological variables is presented in Figure 9. The variables include near-
413 surface air temperature at 2 m AGL (T_{2m}), pressure (Ps), RH, and WD, which are
414 extracted from the first level in sounding. The first level is assumed to be associated
415 with the near-surface variables (Serreze *et al*., 1992; Wang and Wang 2016). We note
416 that BLH, T_{2m}, RH and WD all have substantial diurnal and seasonal variability as
417 partly expressed in Eq. (2).

418 Relatively high positive (negative) correlation coefficients can be noticed between
419 BLH and T_{2m} (RH), with mean values of 0.39/-0.51 (Figure 9a, c), implying that both
420 T_{2m} and RH could be an adequate indicator for the temporal variation of BLH.
421 Moreover, the correlations between BLH and WD are also positively notable, with a
422 mean value of 0.24 (Figure 9d). By contrast, the correlation between Ps and BLH can
423 be ignored above most of the regions (Figure 9b).

https://doi.org/10.5194/acp-2021-257
Preprint. Discussion started: 17 May 2021


Atmospheric Chemistry and Physics Discussions

424 The correlation analyses between BLH and normalized heat fluxes, which are
425 assessed by EAR-5 reanalysis products, are displayed in Figure 10. It is notable that
426 positive/negative correlation coefficients usually exist in normalized sensible/latent
427 heat flux, with a global mean of 0.29 and -0.31. This correlation is not high because
428 BLH also depends on the radiative heating/cooling and the temperature profile in
429 different stations (Yang *et al*., 2004).

430 For the climatological variation of BLH, the near surface variables such as T_{2m},
431 RH and WS, and the normalized sensible/latent heat flux could be a good indicator.
432 Conversely, the development of BLH could also limit the magnitude of RH (McGrath-
433 Spanglerm, 2016).

434 *3.4 Potential sources for the bias between radiosonde and reanalysis products*

435 The possible sources for the difference between radiosonde and reanalysis could
436 be rather complicated. From the spatial pattern of BLH discrepancy results between
437 radiosonde and reanalysis (Figures 5–8), we can notice that the regions with large
438 differences tend to be observed over regions with high elevation, such as the TP in
439 China and Rocky mountain in the U.S. These regions generally have much more
440 complex orography. Coincidently, the soundings over the above-mentioned two regions
441 are all obtained from afternoon, in which the PBL develops to the maximum (Figure 4).
442 As expected, highest biases generally are accompanied with peak BLHs, which has also
443 been confirmed in our previous studies (cf. Figure 2c in Li *et al*., 2017). Therefore, the
444 biases depend on the LST when the weather balloon is launched, which at least could
445 not be ruled out.

446 In addition, the large differences primarily appear in the low and middle latitudes,
447 where thermal convection frequently occurs. Therefore, it is reasonable to infer that
448 static stability could exert an influence on the comparison results. Then, we will analyze
449 the probable influences from terrain and static stability on BLH differences.

450 We evaluate the influence from the orographic complexity around the sounding
451 station and calculate the standard derivation (STD) of elevation within 1°x1° grid, with

https://doi.org/10.5194/acp-2021-257
Preprint. Discussion started: 17 May 2021


Atmospheric Chemistry and Physics Discussions

452 the help of 30 arc second digital elevation model (DEM) dataset. The analysis of the
453 correlation between the bias of the BLH and the standard derivation of the DEM is
454 shown in Figure 11. It follows that the influence from the orography appears
455 instrumental, given the correlation coefficient varying from 0.31 to 0.81. Furthermore,
456 the errors or uncertainties in ERA-5 are less easily impacted by the orographic
457 complexity due to the relatively lower correlation coefficient of 0.31 (Figure 11a).

458 Based on the correlation between orographic complexity (manifested by the STD
459 of the DEM) and the bias of a reanalysis relative to radiosonde measurements, it is
460 likely that the performances of MERR-2, JRA-55, and NCEP-2 might be restricted by
461 the complex underlying terrains. One of the reasons could be because global reanalysis
462 with coarse resolution that cannot resolve the sub-grid processes due to topography.
463 However, ERA-5 appears to be less dependent on terrain. In other words, the models
464 used in ERA-5 show sufficient capability and excellent performance in reproducing the
465 atmospheres, particularly in the PBL over complex terrains.

466 Lower tropospheric stability (LTS) is an indicator to describe the thermodynamic
467 state of the lower atmosphere and is defined by the differences in potential temperature
468 at 700 hPa and 1000 hPa (Guo *et al*., 2016). Typically, the smaller the LTS, the more
469 unstable the low troposphere. The mean LTS over each station is defined by the
470 ensemble mean by four reanalysis datasets, and its spatial distribution is depicted in
471 Figure 12. The lower troposphere over the western United States and western China is
472 more unstable compared to the rest of the world, with LTS of around 6K (Figure 11a),
473 which is likely associated with afternoon launch time of weather balloons. According
474 to the correlation between the bias of BLH and the mean LTS, it is clear that the
475 underestimation in BLH by JRA-55 and NCEP-2 products are negatively correlated
476 with LTS, with correlation coefficients of -0.32 and -0.36 (Figure 12b).

477 Besides the LTS, the role of lifted index could be another influential factor. The
478 lifted index is a predictor of latent instability (Galway, 1956), and it is defined as the
479 temperature difference between the environment temperature and an air parcel lifted
480 adiabatically at 500 hPa. The index is computed by the air temperature, RH, and

https://doi.org/10.5194/acp-2021-257
Preprint. Discussion started: 17 May 2021


Atmospheric Chemistry and Physics Discussions

pressure profiles from radiosondes. We calculate the percentage of negative lifted index above each station, which represents the occurrence rate of latent instability that exists in the daytime (Figure 12c). The stations with high probability of strong instability, denoted by $P(\text{lifted index} < 0)$, are predominantly dispersed over the west U.S, the west and south of China, and the Pacific Ocean, reaching a percentage as high as around 70%. These stations are regularly overlapped with great biases in the reanalysis products as shown in Figures 5-8. According to the analysis, it is clear that all four reanalysis products are positively associated with $P(\text{lifted index} < 0)$, with correlation coefficients ranging from 0.34 to 0.47 (Figure 12d). The positive (negative) correlation coefficients in lifted index suggests that the underestimation by reanalysis might be associated with the instability activity in the lower troposphere that has not been adequately represented or simulated by the models used in reanalyses. In light of the surface heating during the day and the growth of the PBL due to air ascent, it is also inferred that afternoon BLHs suffer the greatest errors if this is caused by inadequate air mixing within the free troposphere in models.

4. Conclusions and summary

A climatology of near-global BLH from high-resolution radiosonde measurements has been yielded for the daytime BLH. The high-resolution radiosonde data has a much finer spatial resolution of 5 m or 10 m, compared to that by IGRA, and can establish a finer and more precise structure of the PBL. In addition, direct comparisons among four well-established reanalysis model products have been conducted. The present study adopts over 300 sounding stations with high-resolution, spanning from 2012 to 2019, to investigate the climatological variation of near-global BLH in the daytime and evaluates four model products at the radiosonde sampling.

Notable spatial variation can be observed in the climatological mean of BLH at 0000 and 1200 UTC. In the afternoon, the regions over the Western United States and Western China have the largest BLHs with values as high as 1.7 km, whereas 0000 and

https://doi.org/10.5194/acp-2021-257
Preprint. Discussion started: 17 May 2021


Atmospheric Chemistry and Physics Discussions

508 1200 UTC compare generally to earlier times of day (LST) in the rest of the world with
509 hence lower BLH. In addition, BLHs in the middle and low latitudes are larger than
510 those in high latitudes. The T_{2m} and RH, and the normalized sensible/latent heat flux
511 are a good predictor for the spatio-temporal evolution of BLH. The most important
512 result is we found that all the four reanalysis products generally underestimate the
513 daytime BLH, with a near-global mean varying from around 130 m to 420 m. The
514 largest bias in reanalysis appears over the Western United States and Western China,
515 where the boundary layers grow vigorously in the afternoon. ERA-5 and MERRA-2
516 definitely have better performance than JRA-55 and NCEP-2 in terms of the magnitude
517 of BLH and a higher correlation coefficient with the soundings. The newest version of
518 reanalysis, ERA-5, has the smallest bias and the highest positive correlation relative to
519 radiosondes. The underestimation by NCEP-2 and JRA-55 is robust over some regions,
520 for instance, western China and western U.S, with differences even exceeding 800 m.
521 However, all products can obtain a precise estimate over some regions, for instance,
522 Europe, the eastern U.S, and polar, probably due to morning LST soundings and smaller
523 daytime PBL development. The BLH over the Pacific Ocean is underestimated in all
524 seasons and by all products. The underestimation tends to have a seasonal dependence,
525 i.e., the warm season has a larger underestimation.

526 We investigated two possible sources contributing to the biases, including
527 topography and static stability. The analysis shows that the DEM spread does have a
528 positive correlation with the bias, suggesting that the reanalysis data cannot provide a
529 reliable simulation result under complex terrain conditions. In addition, reanalysis BLH
530 errors tends to be positively correlated with the occurrence rate of unstable air,
531 suggesting that the reanalyses do not accurately determine BLH when the lower
532 troposphere is unstable.

533 Although this study suffers from the inhomogeneous distribution of the radiosonde
534 sites, the climatological BLHs at the near-global scale can help us understand the
535 variation characteristics of BLH in different regions and for different LST. For the first
536 time, we present near-global BLH estimates from high-resolution radiosondes, and

https://doi.org/10.5194/acp-2021-257
Preprint. Discussion started: 17 May 2021


Atmospheric Chemistry and Physics Discussions

537 further conduct a comprehensive comparison of BLH products for four widely used
538 reanalysis datasets using the BLHs derived from the soundings. The findings provide
539 insights into the limitations of reanalysis data and, more importantly, are expected to
540 greatly benefit future research works related to applications of different kinds of
541 reanalysis data in the future.

542

543 Acknowledgements

544 This study is jointly supported by the National Key Research and Development
545 Program of the Ministry of Science and Technology of China under grant
546 2017YFC1501401, the National Natural Science Foundation of China under grant
547 41771399, 41531070 and 41874177, and S&T Development Fund of CAMS
548 (2021KJ008). The authors would like to acknowledge the National Meteorological
549 Information Centre (NMIC) of CMA, NOAA, German Deutscher Wetterdienst
550 (Climate Data Center), U.K Centre for Environmental Data Analysis (CEDA), GRUAN,
551 and the University of Wyoming (http://data.cma.cn/en,
552 ftp://ftp.ncdc.noaa.gov/pub/data/ua/data/1-sec/, https://cdc.dwd.de/portal/,
553 https://catalogue.ceda.ac.uk/,ftp://ftp.ncdc.noaa.gov/pub/data/gruan/processing/level2/
554 RS92-GDP/version-002/, http://weather.uwyo.edu) for providing the high-resolution
555 sounding data. We would like to thank the ECWMF for ERA-5 data
556 (https://cds.climate.copernicus.eu/cdsapp#!/dataset/reanalysis-era5-single-
557 levels?tab=form), GMAO for MERRA-2
558 (https://disc.gsfc.nasa.gov/datasets?keywords=MERRA-2&page=1), NCAR and Japan
559 Meteorological Agency for JRA-55 (https://climatedataguide.ucar.edu/climate-
560 data/jra-55), NOAA for NCEP-2
561 (https://psl.noaa.gov/data/gridded/data.ncep.reanalysis2.html). NASA for 30 arc
562 second digital evaluation height (DEM) data (https://search.earthdata.nasa.gov/).

563

https://doi.org/10.5194/acp-2021-257
Preprint. Discussion started: 17 May 2021


Atmospheric Chemistry and Physics Discussions

References

Anderson, P. S.: Measurement of Prandtl number as a function of Richardson number avoiding self-correlation, *Bound-Layer Meteorol.,* 131, 345–362, https://doi.org/10.1007/s10546-009-9376-4, 2009.

Ao, C. O., Waliser, D. E., Chan, S. K., Li, J.-L., Tian, B., Xie, F., and Mannucci, A. J: Planetary boundary layer heights from GPS radio occultation refractivity and humidity profiles, *J. Geophys. Res. Atmos.,* 117(D16), https://doi.org/10.1029/2012JD017598, 2012

Basha, G., and Ratnam, M. V.: Identification of atmospheric boundary layer height over a tropical station using high resolution radiosonde refractivity profiles: Comparison with GPS radio occultation measurements, *J. Geophys. Res.-Atmos.,* 114, D16101, https://doi.org/10.1029/2008JD011692, 2009.

Basha, G., Kishore, P., Ratnam, M. V., Ravindra Babu, S., Velicogna, I., Jiang, J. H., and Ao, C. O.: Global climatology of planetary boundary layer top obtained from multi-satellite GPS RO observations, *Clim. Dynam.,* 52, 2385–2398. https://doi.org/10.1007/s00382-018-4269-1, 2018

Belmonte Rivas, M. and Stoffelen, A.: Characterizing ERA-Interim and ERA5 surface wind biases using ASCAT, *Ocean Sci.,* 15, 831–852, https://doi.org/10.5194/os-15-831-2019, 2019.

Chen, X., Škerlak, B., Rotach, M. W., Añel, J. A., Su, Z., Ma, Y., and Li, M.: Reasons for the extremely high-ranging planetary boundary layer over the western Tibetan Plateau in winter, *J. Atmos. Sci.,* 2021–2038, https://doi.org/10.1175/JAS-D-15-0148.1, 2016.

Collaud Coen, M., C. Praz, A. Haefele, D. Ruffieux, P. Kaufmann, and Calpini., B.: Determination and climatology of the planetary boundary layer height by in-situ and remote sensing methods as well as the COSMO model above the Swiss plateau, *Atmos. Chem. Phys.,* 14, 15,419–15,462, https://doi.org/10.5194/acp-14-13205-2014, 2014.

https://doi.org/10.5194/acp-2021-257
Preprint. Discussion started: 17 May 2021


Atmospheric Chemistry and Physics Discussions

592 Davy, R., and I. Esau: Differences in the efficacy of climate forcings explained by
593 variations in atmospheric boundary layer depth, *Nat. Commun.,* 7, 11690,
594 https://doi.org/10.1038/ ncomms11690, 2016.
595 de Arruda Moreira, G., J. L. Guerrero-Rascado, J. A. BravoAranda, et al.: Study of the
596 planetary boundary layer by microwave radiometer, elastic lidar and Doppler lidar
597 estimations in Southern Iberian Peninsula, *Atmos. Res.,* 213, 185–195,
598 https://doi.org/10.1016/j.atmosres.2018.06.007, 2018.
599 Galway, J. G.: The lifted index as a predictor of latent instability, *Bull. Am. Meteorol.*
600 *Soc.,* 37, 528–529, 1956
601 Gelaro R, et al.: The modern-era retrospective analysis for research and applications,
602 version 2 (MERRA-2), *J. Climate*, 30, 5419–5454, https://doi.org/10.1175/JCLI-
603 D-16-0758.1, 2017.
604 Gu, J., Zhang, Y. H., Yang, N., and Wang, R.: Diurnal variability of the planetary
605 boundary layer height estimated from radiosonde data, *Earth Planet. Phys.,* 4(5),
606 479–492, http://doi.org/10.26464/epp2020042, 2020.
607 Guo, J., et al.: The climatology of planetary boundary layer height in China derived
608 from radiosonde and reanalysis data, *Atmos. Chem. Phys.,* 16(20), 13309–13319.
609 https://doi.org/10.5194/acp‐16‐13309‐2016, 2016.
610 Guo, J., et al.: Shift in the temporal trend of boundary layer height trend in China using
611 long-term (1979–2016) radiosonde data, *Geophys. Res. Lett.,* 46 (11): 6080-6089,
612 doi: 10.1029/2019GL082666, 2019.
613 Guo, J., et al.: The climatology of lower tropospheric temperature inversions in China
614 from radiosonde measurements: roles of black carbon, local meteorology, and
615 large-scale subsidence, *J. Climate*, 9327–9350, https://doi.org/10.1175/JCLI-D-
616 19-0278.1, 2020.
617 Haack, A., Gerding, M., and Lübken, F.‐J.: Characteristics of stratospheric turbulent
618 layers measured by LITOS and their relation to the Richardson number, *J. Geophys.*
619 *Res.-Atmos.,* 119, 10,605–10,618. https://doi.org/10.1002/2013JD021008, 2014.
620 Hersbach, Hans, et al.: The ERA5 global reanalysis, *Q. J. Roy. Meteor. Soc.,* 146(730),
621 1999–2049, https://doi.org/10.1002/qj.3803, 2020.

https://doi.org/10.5194/acp-2021-257
Preprint. Discussion started: 17 May 2021


Atmospheric Chemistry and Physics Discussions

622 Houchi, K., Stoffelen, A., Marseille, G. J., and De Kloe, J.: Comparison of wind and
623 wind shear climatologies derived from high-resolution radiosondes and the
624 ECMWF model, *J. Geophys. Res.-Atmos.,* 115, D22123,
625 https://doi.org/10.1029/2009JD013196, 2010.
626 King, G. P., Portabella, M., Lin, W., Stoffelen, A.: Correlating extremes in wind and
627 stress divergence with extremes in rain over the Tropical Atlantic, EUMETSAT
628 Ocean and Sea Ice SAF Scientific Report OSI_AVS_15_02, Version 1.0, 2017.
629 Kobayashi, et al.: The JRA-55 reanalysis: General specifications and basic
630 characteristics, *J. Meteor. Soc. Japan*, 93, 5–48, https://doi.org/10.2151/jmsj.2015-
631 001, 2015.
632 Korhonen, K., Giannakaki, E., Mielonen, T., Pfüller, A., Laakso, L., Vakkari, V., Baars,
633 H., Engelmann, R., Beukes, J. P., Van Zyl, P. G., Ramandh, A., Ntsangwane, L.,
634 Josipovic, M., Tiitta, P., Fourie, G., Ngwana, I., Chiloane, K., and Komppula, M.:
635 Atmospheric boundary layer top height in South Africa: measurements with lidar
636 and radiosonde compared to three atmospheric models, *Atmos. Chem. Phys.,* 14,
637 4263–4278, https://doi.org/10.5194/acp-14-4263-2014, 2014.
638 Li, H., Y. Yang, X.-M. Hu, Z. Huang, G. Wang, B. Zhang, and Zhang, T.: Evaluation
639 of retrieval methods of daytime convective boundary layer height based on lidar
640 data, *J. Geophys. Res.-Atmos.,* 122, 4578–4593,
641 https://doi.org/10.1002/2016JD025620, 2017.
642 Liu, S., and Liang, X.-Z.: Observed diurnal cycle climatology of planetary boundary
643 layer height, *J. Climate*, 23(21), 5790–5809.
644 https://doi.org/10.1175/2010JCLI3552.1, 2010
645 Martins, J. P. A., J. Teixeira, P. M. M. Soares, P. M. A. Miranda, B. H. Kahn, V. T.
646 Dang, F. W. Irion, E. J. Fetzer, and Fishbein, E.: Infrared sounding of the trade-
647 wind boundary layer: AIRS and the RICO experiment, *Geophys. Res. Lett*., 37,
648 L24806, https://doi.org/10.1029/2010GL045902, 2010.
649 McGrath-Spangler, E. L.: The impact of a boundary layer height formulation on the
650 GEOS-5 model climate, *J. Geophys. Res.-Atmos.,* 121, 3263–3275,
651 https://doi.org/10.1002/2015JD024607, 2016.

https://doi.org/10.5194/acp-2021-257
Preprint. Discussion started: 17 May 2021


Atmospheric Chemistry and Physics Discussions

652 McGrath-Spangler, E. L., and Denning, A. S.: Estimates of North American
653 summertime planetary boundary layer depths derived from space-borne lidar, *J.*
654 *Geophys. Res.-Atmos.*, 117, D15101, https://doi.org/10.1029/2012JD017615, 2012.
655 Oliveira, M. I. et al.: Planetary boundary layer evolution over the Amazon rainforest in
656 episodes of deep moist convection at the Amazon Tall Tower Observatory, *Atmos.*
657 *Chem. Phys.*, 20, 15–27, https://doi.org/10.5194/acp-20-15-2020, 2020.
658 Palarz, A., Celiński‐Mysław, D., and Ustrnul, Z.: Temporal and spatial variability of
659 surface‐based inversions over Europe based on ERA-Interim reanalysis, *Int. J.*
660 *Climatol.*, 38(1), 158–168, https://doi.org/10.1002/joc.5167, 2018.
661 Pal, S., and M. Haeffelin, M.: Forcing mechanisms governing diurnal, seasonal, and
662 interannual variability in the boundary layer depths: Five years of continuous lidar
663 observations over a suburban site near Paris, *J. Geophys. Res.-Atmos.,* 120, 11,936–
664 11,956, https://doi.org/10.1002/2015JD023268, 2015.
665 Palm, S. P., A. Benedetti, and Spinhirne, J.: Validation of ECMWF global forecast
666 model parameters using GLAS atmospheric channel measurements, *Geophys. Res.*
667 *Lett.*, 32, L22S09, https://doi.org/10.1029/2005GL023535, 2005.
668 Pithan, F., Angevine, W., and Mauritsen, T.: Improving a global model from the
669 boundary layer: total turbulent energy and the neutral limit Prandtl number, *J. Adv.*
670 *Model. Earth. Syst.,* 7, 791–805, https://doi.org/10 .1002/2014MS000382, 2015.
671 Ratnam, M. V., Basha, G.: A robust method to determine global distribution of
672 atmospheric boundary layer top from COSMIC GPS RO measurements, Atmos.
673 Sci. Lett., 11, 216–222, https://doi.org/10.1002/asl.277, 2010.
674 Rinke, A., Segger, B., Crewell, S., Maturilli, M., Naakka, T., Nygård, T., Vihma, T.,
675 Alshawaf, F., et al.: Trends of vertically integrated water vapor over the arctic
676 during 1979-2016: Consistent moistening all over?, *J. Climate*, 32(18), 6097–6116,
677 https://doi.org/10.1175/JCLI-D-19-0092.1, 2019.
678 Saha, S., Moorthi, S., Wu, X., Wang, J., Nadiga, S., Tripp, P., Behringer, D., Hou, Y.
679 T., Chuang, H.Y., Iredell, M. and Ek, M.: The NCEP climate forecast system
680 version 2, *J. Climate*, 27(6), 2185–2208, https://doi.org/10.1175/JCLI-D-12-
681 00823.1, 2014.

https://doi.org/10.5194/acp-2021-257
Preprint. Discussion started: 17 May 2021


Atmospheric Chemistry and Physics Discussions

682 Scotti, A.: Biases in Thorpe-scale estimates of turbulence dissipation. Part II: energetics
683 arguments and turbulence simulations, *J. Phy. Oceanog.,* 45(10), 2522–2543,
684 https://doi.org/10.1175/JPO-D-14-0092.1, 2015.
685 Seibert, P., Beyrich, F., Gryning, S. E., Joffre, S., Rasmussen, A., and Tercier, P.:
686 Review and inter-comparison of operational methods for the determination of the
687 mixing height, *Atmos. Environ.,* 34, 1001–1027, https://doi.org/10.1016/S1352-
688 2310(99)00349-0, 2000.
689 Seidel, D. J., Ao, C. O., and Li, K.: Estimating climatological planetary boundary layer
690 heights from radiosonde observations: Comparison of methods and uncertainty
691 analysis, *J. Geophys. Res.-Atmos.,* 115(D16),
692 https://doi.org/10.1029/2009JD013680, 2010.
693 Seidel, D. J., Zhang, Y., Beljaars, A., Golaz, J.-C., Jacobson, A. R., and Medeiros, B.:
694 Climatology of the planetary boundary layer over the continental United States and
695 Europe, *J. Geophys. Res.-Atmos.,* 117(D17),
696 https://doi.org/10.1029/2012JD018143, 2012.
697 Serreze, M. C., J. A. Maslanik, M. C. Rehder, R. C. Schnell, J. D. Kahl, and E. L.
698 Andreas, E. L.: Theoretical heights of buoyant convection above open leads in the
699 winter Arctic pack ice cover*, J. Geophys. Res.-Atmos.*, 97, 9411–9422, 1992.
700 Short, E., Vincent, C. L., & Lane, T. P: Diurnal cycle of surface winds in the Maritime
701 Continent observed through satellite scatterometry, *Mon. Weather. Rev.,* 147(6),
702 2023–2044, https://doi.org/10.1175/MWR-D-18-0433.1, 2019.
703 Stull, R. B.: An Introduction to Boundary Layer Meteorology. Kluwer Academic, 666
704 pp, Dordrecht, the Netherlands, 1988.
705 Su, T., Li, Z., and Kahn, R.: Relationships between the planetary boundary layer height
706 and surface pollutants derived from lidar observations over China: regional pattern
707 and influencing factors, *Atmos. Chem. Phys.,* 18, 15921–15935,
708 https://doi.org/10.5194/acp-18-15921-2018, 2018.
709 Su, T., Li, Z., Zheng, Y., Luan, Q., and Guo, J.: Abnormally shallow boundary layer
710 associated with severe air pollution during the COVID‐19 lockdown in China,
711 *Geophys. Res. Lett.,* 47(20), https://doi.org/10.1029/2020GL090041, 2020.

https://doi.org/10.5194/acp-2021-257
Preprint. Discussion started: 17 May 2021


Atmospheric Chemistry and Physics Discussions

712 Taylor, A. C., Beare, R. J., and Thomson, D. J.: Simulating dispersion in the evening-
713 transition boundary layer, *Bound-Layer Meteorol.,* 153, 389–407,
714 https://doi.org/10.1007/s10546-014-9960-0, 2014.
715 von Engeln, A., and Teixeira, J.: A planetary boundary layer height climatology derived
716 from ECMWF reanalysis data, *J. Climate*, 26(17), 6575–6590,
717 https://doi.org/10.1175/JCLI-D-12-00385.1, 2013.
718 Wang, X., and Wang, K.: Homogenized variability of radiosonde-derived atmospheric
719 boundary layer height over the global land surface from 1973 to 2014. *J. Climate*,
720 29, 6893–6908, https://doi.org/10.1175/JCLI-D-15-0766.1, 2016.
721 Wei, N., Zhou, L., and Dai, Y.: Evaluation of simulated climatological diurnal
722 temperature range in CMIP5 models from the perspective of planetary boundary
723 layer turbulent mixing, *Clim. Dynam.,* 49, 1–22, https://doi.org/10.1007/s00382 -
724 016 - 3323 - 0, 2017.
725 Yang, K., T. Koike, H. Fujii, T. Tamura, X. Xu, L. Bian, and Zhou, M.: The Daytime
726 Evolution of the Atmospheric Boundary Layer and Convection over the Tibetan
727 Plateau: Observations and Simulations, J. Meteorol.Soc.Jpn., 82 (6), 1777-1792,
728 2004.
729 Zhang, Y., Sun, K., Gao, Z., Pan, Z., Shook, M. A., and Li, D.: Diurnal climatology of
730 planetary boundary layer height over the contiguous United States derived from
731 AMDAR and reanalysis data, *J. Geophys. Res.-Atmos.,* 125,
732 https://doi.org/10.1029/2020JD032803, 2020a.
733 Zhang, Y., J. Guo, Y. Yang, Y. Wang, and S.H.L. Yim: Vertical wind shear modulates
734 particulate matter pollutions: A perspective from Radar wind profiler observations
735 in Beijing, China, *Remote Sens.,* 12(3), 546. https://doi.org/10.3390/rs12030546,
736 2020b.
737 Zhang, W., Guo, J., Miao, Y., Liu, H., Li, Z., and Zhai, P.: Planetary boundary layer
738 height from CALIOP compared to radiosonde over China, *Atmos. Chem. Phys.,* 16,
739 9951–9963, https://doi.org/10.5194/acp-16-9951-2016, 2016.
740 Zhang, W., Guo, J., Miao, Y., Liu, H., Song, Y., Fang, Z., He, J., Lou, M., Yan, Y., Li,
741 Y., and Zhai, P.: On the summertime planetary boundary layer with different

https://doi.org/10.5194/acp-2021-257
Preprint. Discussion started: 17 May 2021

742 thermodynamic stability in China: A radiosonde perspective, *J. Climate*, 31(4),
743 1451–1465, https://doi.org/10.1175/JCLI-D-17-0231.1, 2018.
744 Zhang, J., Zhang, S. D., Huang, C. M., Huang, K. M., Gong, Y., Gan, Q., and Zhang,
745 Y. H.: Latitudinal and topographical variabilities of free atmospheric turbulence
746 from high‐resolution radiosonde data sets, *J. Geophys. Res.-Atmos.,* 124, 4283–
747 4298, https://doi.org/10.1029/2018JD029982, 2019.
748 Zhang, Y., D. J. Seidel, J.-C. Golaz, C. Deser, and Tomas, R. A.: Climatological
749 characteristics of Arctic and Antarctic surface-based inversions, *J. Climate*, 24,
750 5167–5186, https://doi.org/10.1175/2011JCLI4004.1, 2011.
751 Zhang, Y. H., Seidel, D. J., and Zhang, S. D.: Trends in planetary boundary layer height
752 over Europe, J. Climate, 26(24), 10,071–10,076, https://doi.org/10.1175/JCLI‐
753 D‐13‐00108.1, 2013.
754 Zilitinkevich, S., and Baklanov, A.: Calculation of the height of the stable boundary
755 layer in practical applications, *Bound-Layer Meteorol.,* 105(3), 389–409.
756 https://doi.org/10.1023/A:1020376832738, 2002.
757
758

https://doi.org/10.5194/acp-2021-257
Preprint. Discussion started: 17 May 2021

Atmospheric Chemistry and Physics Discussions

759 **Figures:**

760

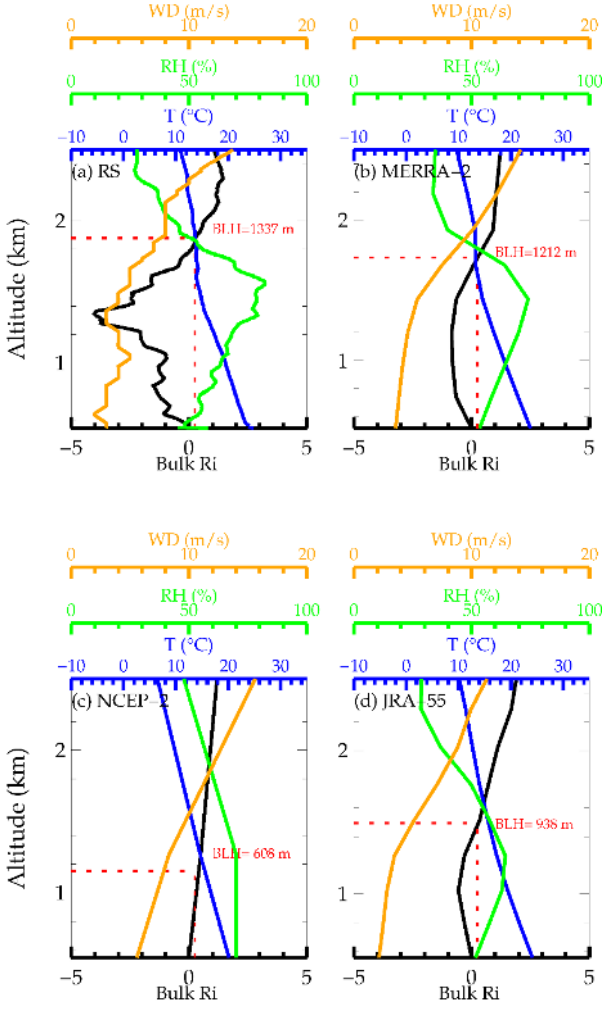

761

762 **Figure 1**. Profiles of basic atmomospheric parameters from the ground up to 2.5 km
763 AGL, including wind speed (orange), bulk Ri (black), temperature (blue), and RH
764 (green) at 0500 UTC (13 LST) 06 Jun 2016 at Chongqing (29.6°N, 106.4°E) from
765 radiosonde (a), MERRA-2 (b), NCEP-2 (c), and JRA-55 (d) reanalysis datasets. Note
766 that the boundary layer height in each subplot is marked by red dash lines and red texts,
767 and the BLH for ERA-5 is 1265m in this case.

768

https://doi.org/10.5194/acp-2021-257
Preprint. Discussion started: 17 May 2021

Atmospheric Chemistry and Physics Discussions

769

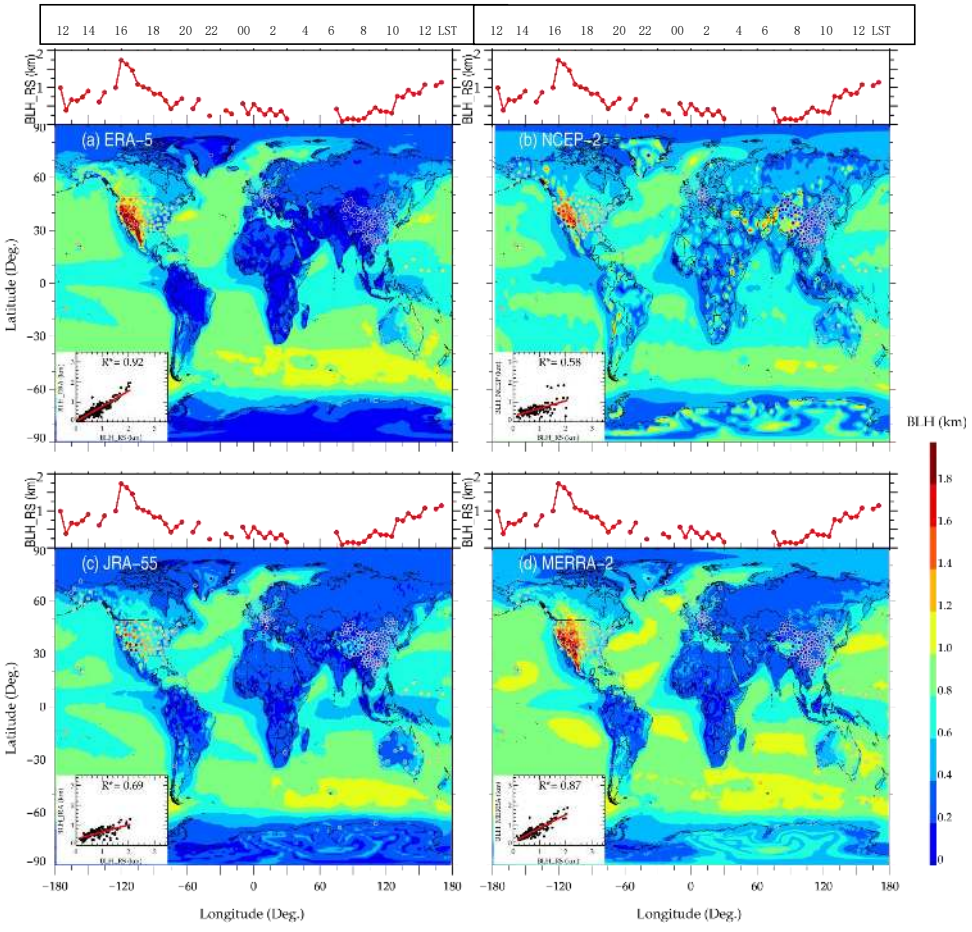

770

771 **Figure 2**. The ensemble mean BLH estimated from ERA-5 (a), NCEP-2 (b), JRA-55
772 (c), and MERRA-2 (d) reanalysis data at 0000 UTC during years 2012 − 2019. The dots
773 with gray marginal lines in each map denote the mean BLH derived by sondes at 0000
774 UTC, and the red dotted lines present the mean BLH derived by radiosonde on a grid
775 with 5° longitude. Stations with less than 10 profiles are not included in the analysis.
776 The 2D scatter plot in the left bottom corner of each panel illustrates the correlations
777 between reanalysis-derived and sonde-derived BLHs at 0000 UTC, where the asterisk
778 (*) superscripts indicate that the correlation coefficients are statistically significant
779 ($p<0.05$) and the red lines denote the least-squares regression line.

780

https://doi.org/10.5194/acp-2021-257
Preprint. Discussion started: 17 May 2021

Atmospheric Chemistry and Physics Discussions

781

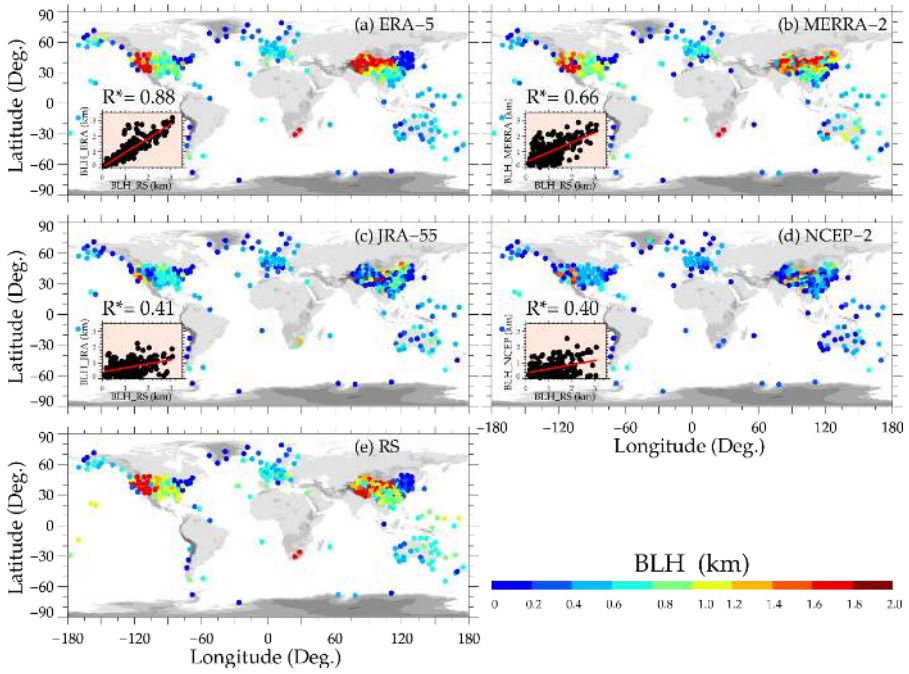

782

783 **Figure 3**. Spatial distributions of the mean BLHs determined at the near-global high-
784 resolution radiosonde observational network locations during the daytime for the period
785 2012 to 2019, which is extracted from ERA-5 (a), MERRA-2 (b), JRA-55 (c), NCEP-
786 2 (d), and radiosonde measurements (e), respectively. Similar to Figure 2, the scatter
787 plot illustrates the correlations between reanalysis-derived and sonde-determined BLHs
788 in the daytime.

789

790

791

https://doi.org/10.5194/acp-2021-257
Preprint. Discussion started: 17 May 2021

Atmospheric Chemistry and Physics Discussions

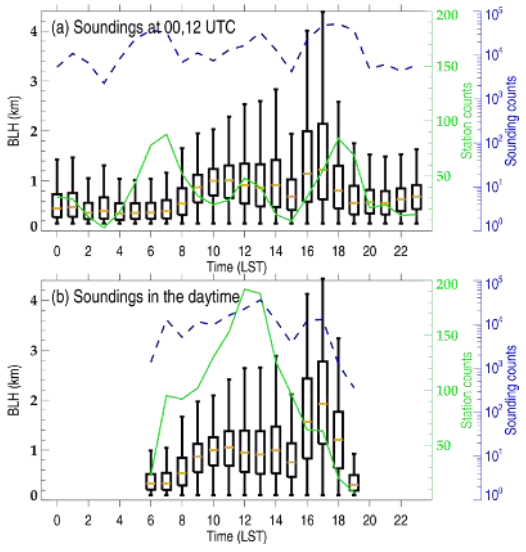

792

793 **Figure 4.** Box and whisker plots of diurnal variation (in LST, 24 hours) of BLH
794 determined by all soundings operationally launched at 0000 and 1200 UTC (a) and by
795 the soundings launched at both synoptic times and intensive observation times that are
796 limited to the daytime alone (b). Solid green line and dotted blue line highlight the
797 number of sonde station and total sounding for each hour of day, respectively.

798

799

https://doi.org/10.5194/acp-2021-257
Preprint. Discussion started: 17 May 2021

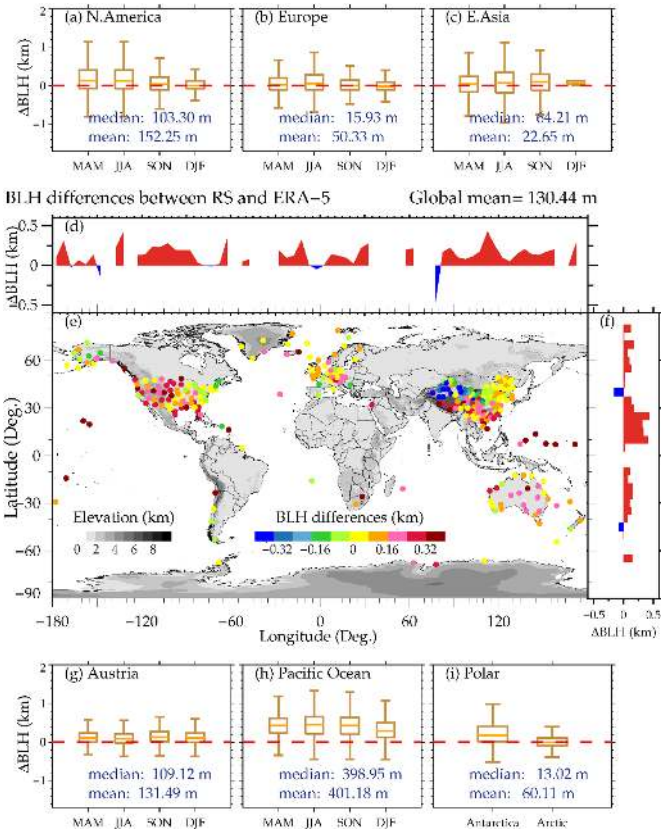

Figure 5. Statstical results of BLH differences between radiosonde and ERA-5. The spatial distribution of mean differences is highlighted in (e). Also shown are the distributions of mean BLH differences as a function of longitude (d) and latitude (f). The box and whisker plot of BLH differences over the six regions of interest (i.e., North America, Europe, East Asia, Austria, Pacific Ocean, Polar) over four seasons are displayed in (a-c), (g-i). The seasons are defined as follows: MAM, March–April–May; JJA, June–July–August; SON, September–October–November; DJF, December–January–February.

https://doi.org/10.5194/acp-2021-257
Preprint. Discussion started: 17 May 2021

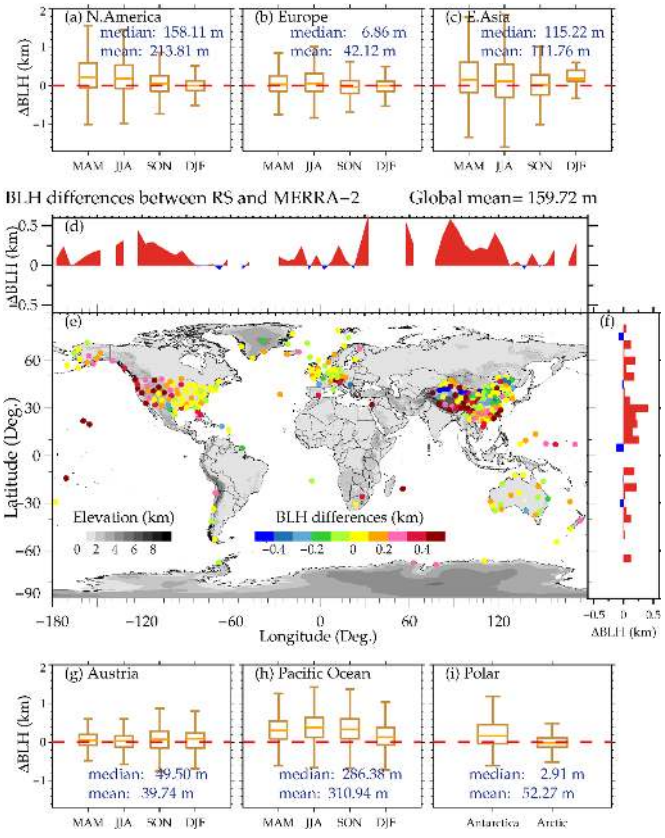

Figure 6. Similar as Figure 5, but for the differences between radiosonde-determined BLHs and MERRA-2-derived BLHs.

https://doi.org/10.5194/acp-2021-257
Preprint. Discussion started: 17 May 2021

Atmospheric Chemistry and Physics Discussions

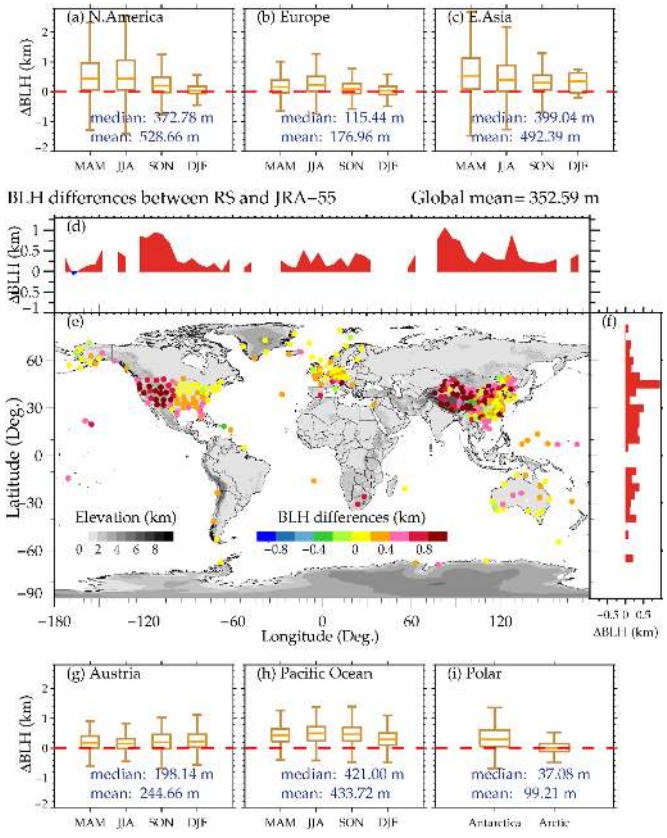

Figure 7. Similar as Figure 5, but for the differences between radiosonde-determined BLHs and JRA-55-derived BLHs.

https://doi.org/10.5194/acp-2021-257
Preprint. Discussion started: 17 May 2021

Atmospheric Chemistry and Physics Discussions

840

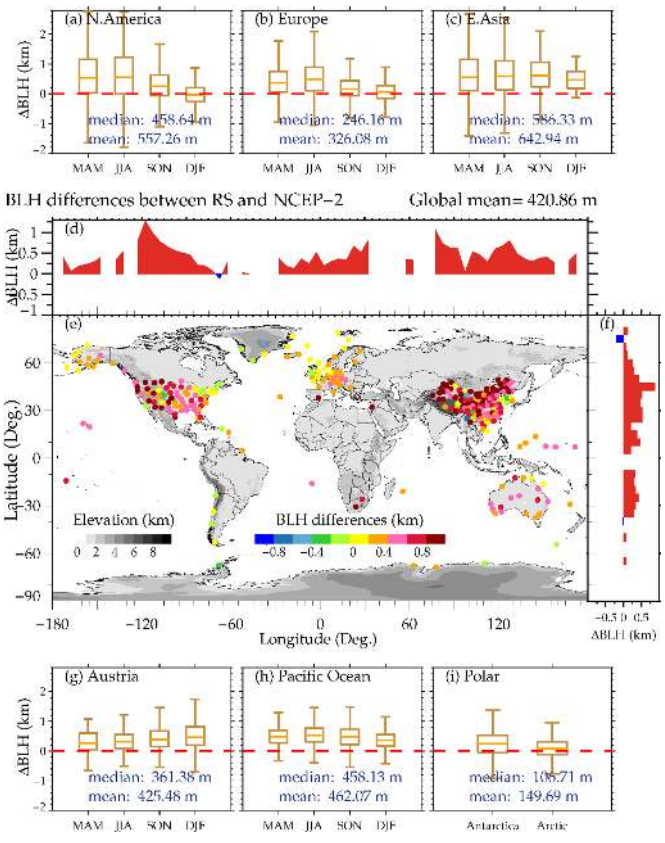

841

842 **Figure 8**. Similar as Figure 5, but for the differences between radiosonde-determined

843 BLHs and NCEP-2-derived BLHs

844

845

846

847

848

849

850

851

852

853

https://doi.org/10.5194/acp-2021-257
Preprint. Discussion started: 17 May 2021

Atmospheric Chemistry and Physics Discussions

854

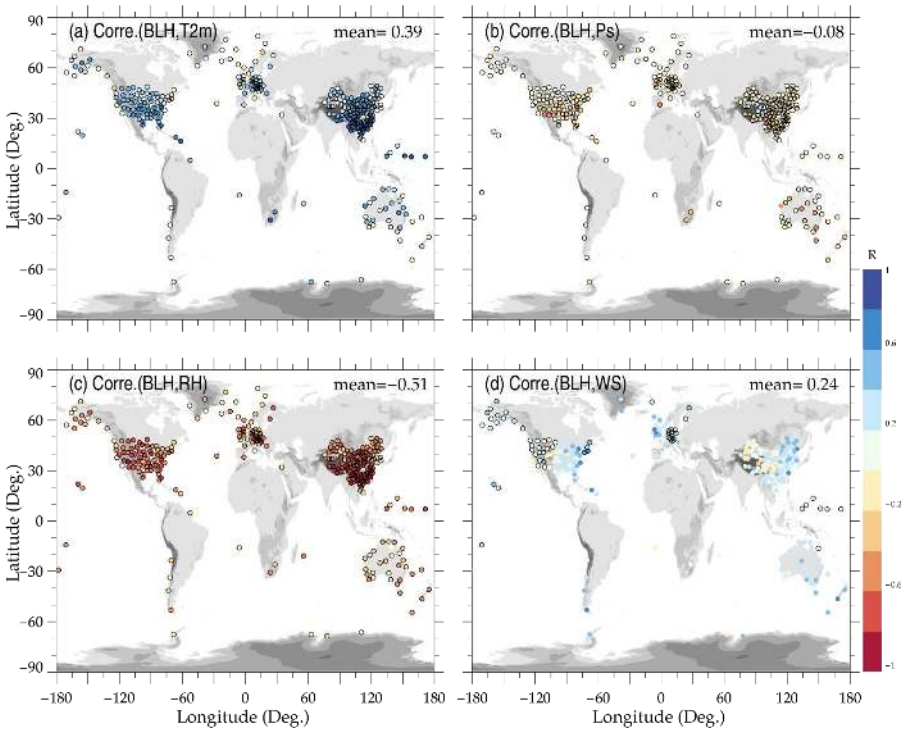

855

856 **Figure 9.** Correlations between the radiosonde-derived BLHs and near-surface air
857 temperature at 2m AGL (T_{2m}; a), near-surface pressure (Ps; b), near-surface RH (c),
858 and near-surface wind speed (WS; d). Dots outlined in black denote that the correlation
859 coefficient values are statistically significant ($p<0.05$), and the mean correlations are
860 texted in the upper right corner of each panel.

861

862

863

864

865

866

867

868

869

https://doi.org/10.5194/acp-2021-257
Preprint. Discussion started: 17 May 2021

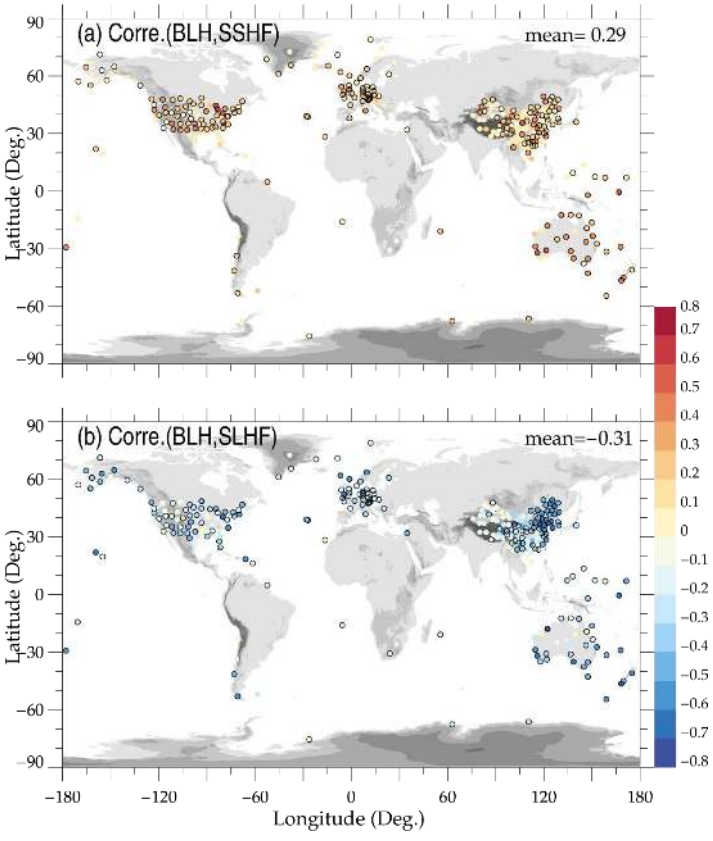

Figure 10. Similar as Figure 8, but for the correlations between BLHs versus normalized surface sensible (a) and latent heat fluxes (b).

https://doi.org/10.5194/acp-2021-257
Preprint. Discussion started: 17 May 2021

Atmospheric Chemistry and Physics Discussions

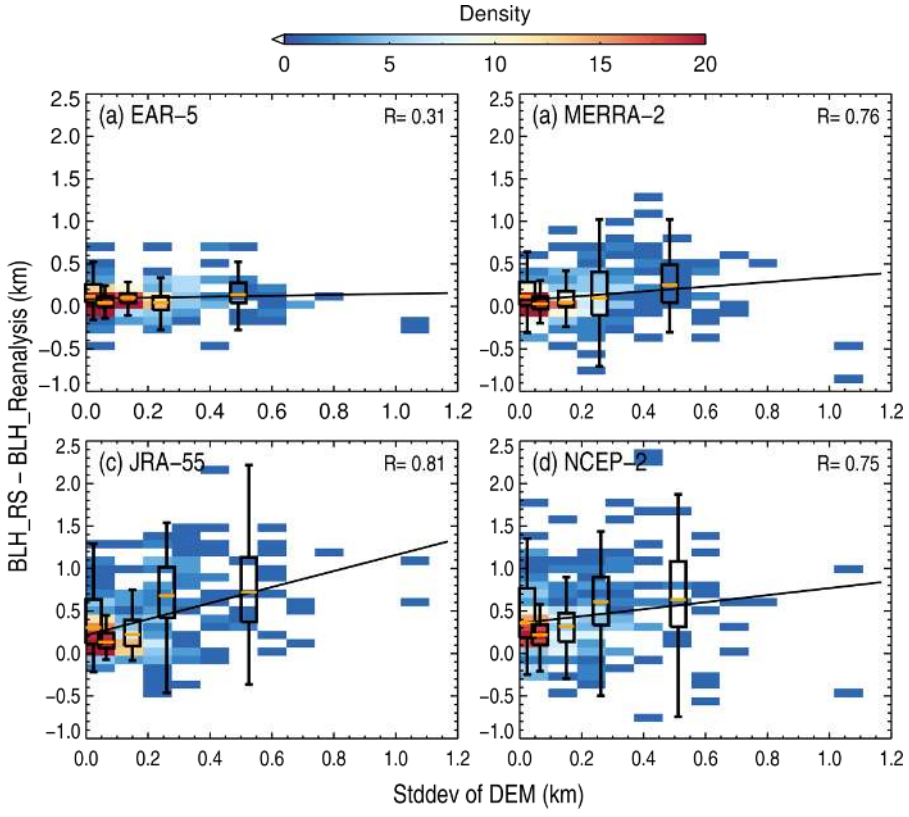

Figure 11. Density plots of the differences of BLHs between radiosonde and ERA-5 (a), MERRA-2 (b), JRA-55 (c), and NCEP-2 (d) as a function of the standard derivation of the DEM, where the black lines denote the least-squares regression line. The box-and-whisker plots of the anomalies of BLH in five evenly intervals are overlaid in each panel, and the correlation coefficients are marked in the upper right corner of each panel.

https://doi.org/10.5194/acp-2021-257
Preprint. Discussion started: 17 May 2021

Atmospheric Chemistry and Physics Discussions

894

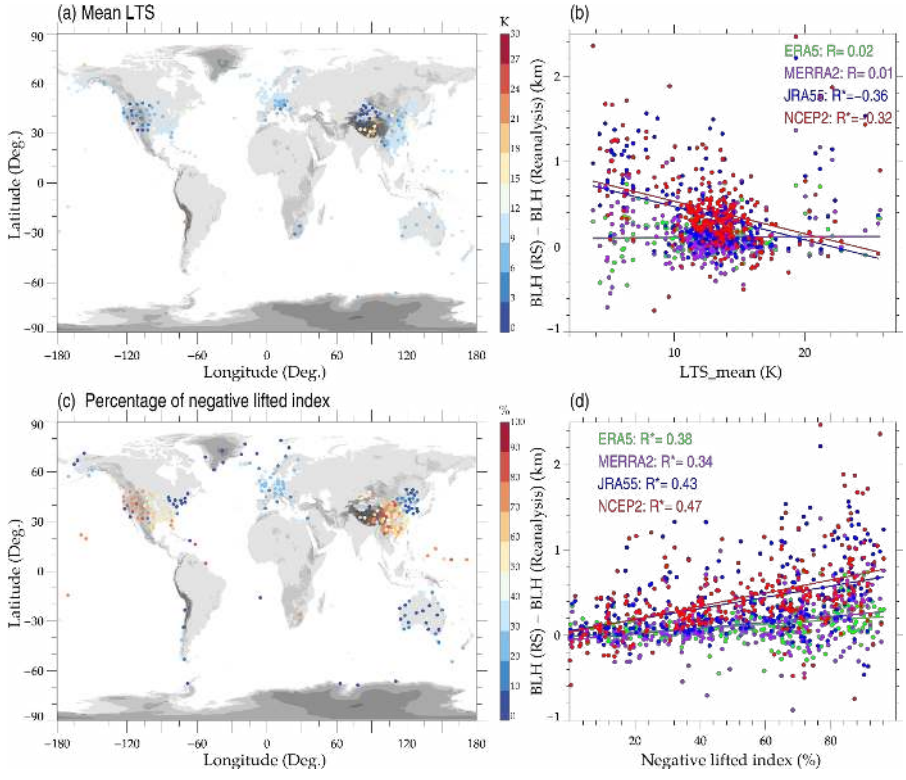

895

896 **Figure 12**. Spatial distribution of the ensemble means of lower tropospheric stability in
897 the daytime (a). The scatter plots showing the difference of sounding- minus model-
898 derived BLHs from four reanalysis datasets versus the anomalies of LTS as derived
899 from four reanalysis relative to those from soundings (b). The variations in the
900 percentage of negative lifted index (c), and the anomalies of BLH as a function of
901 negative lifted index (d).